

# Ultraflatbands and Shear Solitons in Moiré Patterns of Twisted Bilayer Transition Metal Dichalcogenides

Mit H. Naik and Manish Jain\*

Center for Condensed Matter Theory, Department of Physics, Indian Institute of Science, Bangalore 560012, India

(Received 29 March 2018; revised manuscript received 26 July 2018; published 28 December 2018)

Ultraflatbands in twisted bilayers of two-dimensional materials have the potential to host strong correlations, including the Mott-insulating phase at half-filling of the band. Using first-principles density functional theory calculations, we show the emergence of ultraflatbands at the valence band edge in twisted bilayer MoS<sub>2</sub>, a prototypical transition metal dichalcogenide. The computed band widths, 5 and 23 meV for 56.5° and 3.5° twist angles, respectively, are comparable to that of twisted bilayer graphene near “magic” angles. Large structural transformations in the moiré patterns lead to formation of shear solitons at stacking boundaries and strongly influence the electronic structure. We extend our analysis for twisted bilayer MoS<sub>2</sub> to show that flatbands can occur at the valence band edge of twisted bilayer WS<sub>2</sub>, MoSe<sub>2</sub>, and WSe<sub>2</sub> as well.

DOI: 10.1103/PhysRevLett.121.266401

Combining bilayers of two-dimensional materials with a small-angle twist between the layers or combining two dissimilar 2D materials with a small lattice mismatch leads to the formation of moiré superlattices (MSL) with periodicity in the order of nanometers [1–3]. MSLs in twisted bilayer graphene (TBLG) host a plethora of fascinating physics at the structural [1,4,5] and electronic level [6–11]. Rearrangement of atoms in the MSL leads to the formation of shear solitons and topological point defects [1,5,12,13]. The electronic structure of these MSLs can be different from that of the constituent layers, like formation of flatbands and localization of states close to the Fermi level [12,14–17]. Probing flatbands in TBLG has recently led to the discovery of unconventional superconductivity close to a magic angle. [16–19].

MoS<sub>2</sub>, a 2D transition metal dichalcogenide (TMD), is arguably the most popular 2D material after graphene [20–22]. Because of its semiconducting nature, extensive applications in electronics and optoelectronics have been explored [21–23]. However, in contrast to TBLG, MSLs in twisted bilayer MoS<sub>2</sub> (TBLM) have not received as much attention [24–30]. In this Letter, we use first-principles density functional theory (DFT) [31] calculations to study the electronic and structural transformations in the MSLs of TBLM. We show a large structural reconstruction in the moiré pattern, leading to the formation of shear solitons and ultraflatbands at the valence band edge of TBLM. These flatbands have bandwidths comparable to those observed in TBLG close to magic angles [16,17]. Our calculations show that in-plane relaxations of the layers drive the out-of-plane relaxations, which in turn lead to localization of the VBM. We show that the spatial localization of the flatband significantly changes if the bilayers are rigidly twisted and

relaxations are ignored. Localization of the flatband can influence exciton dynamics and binding energy in the moiré pattern. The ratio of on site Coulomb interaction to bandwidth of the flatband is found to be large, indicating the possibility of a Mott-insulating phase at half-filling of the band.

TBLM forms two distinguishable MSLs for small twist angles close to 0° and close to 60°. For TBLG, these are equivalent. Figures 1(a) and 1(e) show the MSLs formed

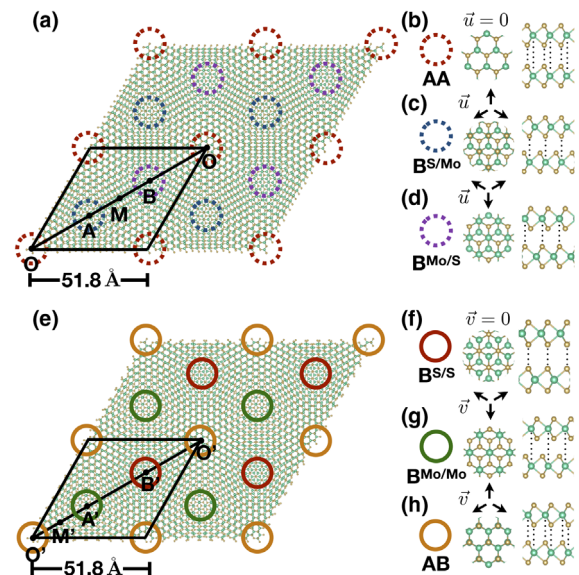


FIG. 1. (a),(e) Moiré superlattice formed by twisting bilayer MoS<sub>2</sub> by 3.5° and 56.5°, respectively. The high-symmetry stackings are highlighted in these superlattices using circles. The stacking within the circle is shown in (b)–(h). The direction of the order parameter,  $\vec{u}$  or  $\vec{v}$  (see text for details), is also shown.

for twist angle  $3.5^\circ$  ( $M^{3.5}$ ) and  $56.5^\circ$  ( $M^{56.5}$ ), respectively. These superlattices are composed of various high-symmetry stackings. We define  $B^{X/Y}$  as being a Bernal-like stacking of the two layers with the  $X$  atom in the top layer directly above the  $Y$  atom in the bottom layer.  $M^{3.5}$  consists of the  $AA$  stacking,  $B^{S/Mo}$  and  $B^{Mo/S}$  (Fig. 1).  $M^{56.5}$  similarly consists of the  $B^{S/S}$ ,  $B^{Mo/Mo}$ , and  $AB$  (Fig. 1) stackings. We note that no simple translation transforms the  $AA$  stacking to  $AB$  stacking. We define an order parameter  $\vec{u}$  [1,12] for twist angles close to  $0^\circ$  as the shortest displacement vector that takes any given stacking to the highest energy stacking in the corresponding moiré pattern:  $AA$  stacking in this case. For twist angle close to  $60^\circ$ , we define  $\vec{v}$  as the shortest displacement vector that takes any given stacking to the highest energy stacking  $B^{S/S}$ .

All the DFT calculations are performed using the pseudopotential plane wave package, QUANTUM ESPRESSO [32]. We simulate the following angles in this study:  $3.5^\circ$ ,  $5.1^\circ$ ,  $7.3^\circ$ ,  $56.5^\circ$ ,  $54.9^\circ$ , and  $52.7^\circ$  [33,34]. The code TWISTER [35] is used to generate the atom positions for these structures.  $M^{3.5}$  and  $M^{56.5}$  are the largest systems in our calculation, containing 1626 atoms. In all MSL calculations, the Brillouin zone is sampled at the  $\Gamma$  point to obtain the self-consistent charge density. The Hamiltonian is subsequently constructed and diagonalized at other  $k$  points in the Brillouin zone to obtain the band structure (see Supplemental Material for more details [36]).

To understand the relaxation in the MSL, we study the relative energies of the stackings keeping the interlayer spacing (ILS) fixed at  $5.9 \text{ \AA}$ . The relative total energy per unit  $\text{MoS}_2$  along the line traversing high-symmetry stackings [defined in Figs. 1(a) and 1(e)] in  $M^{3.5}$  and  $M^{56.5}$  is shown in Fig. 2(a). The  $AA$  ( $O$  point) and  $B^{S/S}$  ( $B'$  point) stackings have S atoms of the top layer directly above the S atoms in the bottom layer. Strong repulsion between the out-of-plane  $S-p_z$  orbitals causes these stackings to have the highest energy. Stackings with S on top of Mo are energetically favorable. On relaxing the MSLs, large structural transformations with respect to the rigidly twisted bilayer are observed. The out-of-plane displacements of these relaxation patterns lead to local variations in the ILS between the two layers. Figure 2(a) shows the ILS in  $M^{3.5}$  and  $M^{56.5}$  along the line defined in Figs. 1(a) and 1(e). The relative energies correlate strongly with the ILS. The variation in the ILSs increases as the twist angles approach  $0^\circ$  or  $60^\circ$  [Fig. 2(b)]. The local ILS is maximum in the  $AA$  ( $B^{S/S}$ ) stacked patches for  $M^{3.5}$  ( $M^{56.5}$ ) and is comparable to that of the isolated  $AA$  ( $B^{S/S}$ ) stacking. The ILS is smallest for the  $B^{Mo/S}$  ( $B^{Mo/Mo}$ ) and  $B^{S/Mo}$  stackings ( $AB$ ) in  $M^{3.5}$  ( $M^{56.5}$ ). This variation in ILS in TBLM ( $\sim 0.6 \text{ \AA}$ ) is much larger than TBLG ( $\sim 0.2 \text{ \AA}$ ) [12]. To understand the coupling between the in-plane and out-of-plane displacements, we relax the TBLM, keeping the in-plane positions

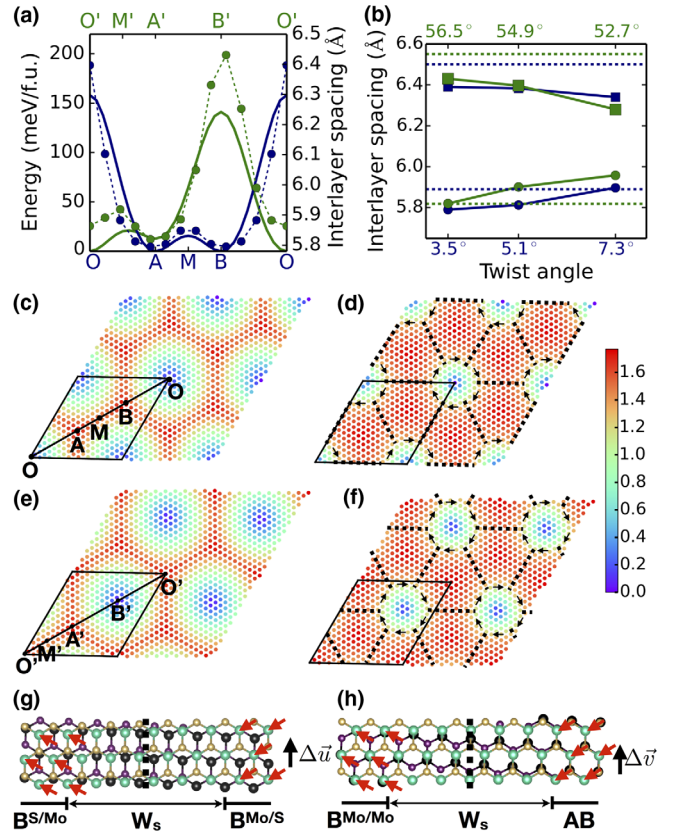


FIG. 2. (a) The relative energy and ILS of the stackings along a line in the MSL. The blue (green) lines corresponds to the path in  $M^{3.5}$  ( $M^{56.5}$ ). The solid (dashed) lines represent the relative total energy (ILS) along the path. (b) Maximum (squares) and minimum (circles) ILS in the MSL as a function of twist angle. The green and blue lines correspond to angles approaching  $60^\circ$  and  $0^\circ$ , respectively. The dashed lines represent the maximum and minimum equilibrium ILS of the corresponding isolated stackings. Distribution of  $|\vec{u}|$  and  $|\vec{v}|$  in the (c),(e) unrelaxed and (d), (f) relaxed MSLs. The dashed lines denote stacking boundaries. The arrows in (d) and (f) denote the direction of order parameters. (g),(h) Structure, order parameter (red arrows), and the change in order parameter across a stacking boundary.

of the atoms fixed (i.e., no in-plane shear) to that of the rigidly twisted bilayer. On adding this constraint, the variation in the ILS across the MSLs is significantly reduced (see Supplemental Material [36]).

The order parameter vectors,  $\vec{u}$  and  $\vec{v}$ , are computed locally for every Mo atom in  $M^{3.5}$  and  $M^{56.5}$ , respectively. The spatial variation of  $|\vec{u}|$  and  $|\vec{v}|$  for rigidly TBLM is shown in Figs. 2(c) and 2(e).  $|\vec{u}| = 0$  and  $|\vec{v}| = 0$  for  $O$  ( $AA$ ) and  $B'$  ( $B^{S/S}$ ) regions, as defined.  $|\vec{u}|$  takes a maximal value of  $1.8 \text{ \AA}$ , i.e., the in-plane Mo-S distance, for  $A$  ( $B^{S/Mo}$ ) and  $B$  ( $B^{Mo/S}$ ) regions. Similarly,  $|\vec{v}| = 1.8 \text{ \AA}$  for  $O'$  ( $AB$ ) and  $A'$  ( $B^{Mo/Mo}$ ) regions. Thus, large values of  $|\vec{u}|$  and  $|\vec{v}|$  indicate regions of low energy [Fig. 2(a)]. On relaxing the structure, the  $\text{MoS}_2$  units in the top layer and bottom layer displace in opposite directions in-plane,

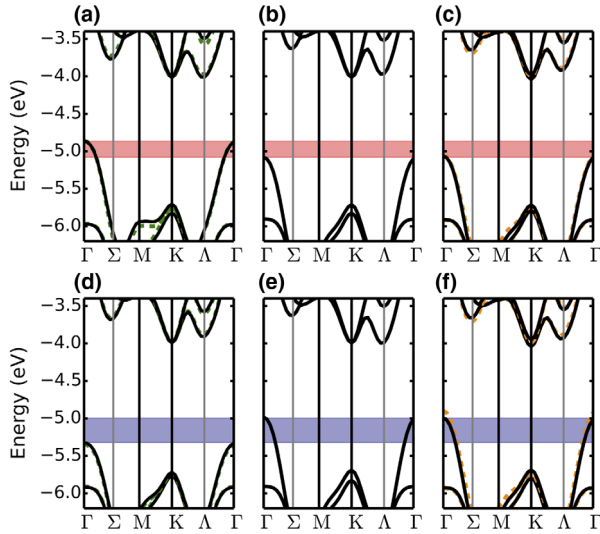


FIG. 3. (a)–(c) Band structures of the isolated high-symmetry stackings with interlayer spacing fixed at 5.9 Å. AA and  $B^{S/S}$  are shown in (a) with a black solid line and green dashed line, respectively. AB is shown in (b) with a black solid line.  $B^{Mo/S}$  and  $B^{Mo/Mo}$  are shown in (c) with a black solid line and orange dashed line, respectively. In the same order and colors, (d)–(f) show the band structures at their equilibrium ILS. The blue or red shaded region marks the difference in VBM energy between  $B^{Mo/S}$  and AA stackings.

forming a vortexlike pattern around the  $O$  and  $B'$  points (see Supplemental Material [36]). These in-plane displacements in  $M^{3.5}$  and  $M^{56.5}$  increase the fractional area of the respective low-energy stackings. The large variation in the distribution of  $|\vec{u}|$  and  $|\vec{v}|$  as shown in Figs. 2(d) and 2(f) from the rigidly TBLM is indicative of this transformation.

A domain boundary separates adjacent low-energy stackings, denoted by the dashed lines in Figs. 2(d) and 2(f). A similar transformation is observed in TBLG for small twist angles, leading to the formation of triangular domains of Bernal stackings, with the AA stacking at the vertices of the triangles [1,12]. A shift (change in the order parameter) in the relative registry of the atoms is necessary to traverse across the boundary. This change in the order parameter is parallel to the domain boundary, indicating a shear-strain soliton [1]. Figures 2(g) and 2(h) show the shear-strain soliton between  $B^{S/Mo}$  and  $B^{Mo/S}$  stackings in  $M^{3.5}$  and between AB and  $B^{Mo/Mo}$  in  $M^{56.5}$ , respectively. The width of the soliton is  $\sim 1.5$  nm,  $W_s$ . The soliton width is expected to be larger for smaller angles and to ultimately saturate [12] for vanishing angles. Furthermore, the order parameter in the vicinity of the  $O$  ( $\vec{u} = 0$ ) and  $B'$  ( $\vec{v} = 0$ ) points rotates by  $2\pi$  [see Figs. 2(d) and 2(f)]. These points are thus topological point defects [1].

The electronic structure of the MSLs can be understood in terms of the constituent high-symmetry stackings. The band structure of bilayer MoS<sub>2</sub> (BLM) is sensitive to stacking and ILS. Figure 3 shows the band structure of

the five high-symmetry stackings. The VBM in all BLM stackings is at the  $\Gamma$  point, unlike bilayer graphene, where it is at the  $K$  point. The band structure close to the Fermi level, for all stackings, shows large band splittings at the  $\Gamma$  point and relatively small splittings at the  $K$  point. This is indicative of the strength of hybridization between the two layers at these points. The  $K$  and  $\Gamma$  point wave functions close to the Fermi level in monolayer MoS<sub>2</sub> have small and large spreads in the out-of-plane direction, respectively [45]. This spread determines the hybridization, leading to the different splittings.

Among the band structures of stackings shown in Figs. 3(a)–3(c), AA and  $B^{S/S}$  show the largest splittings at the  $\Gamma$  point VBM [Fig. 3(a)]. This is due to the close proximity of the S atoms in these stackings. Note that the ILS is fixed at 5.9 Å for these band structures, the same as that for rigidly TBLM. The effect of these large splittings is that the VBM (with respect to the vacuum level) of the AA and  $B^{S/S}$  stackings is higher ( $\sim -4.8$  eV) than the rest of the stackings ( $\sim -5.1$  eV). In the rigidly twisted  $M^{3.5}$ , the unit cell band structure of each layer is folded into the Brillouin zone of the MSL (TBZ). Thus, the VBM of  $M^{3.5}$ , which contains both AA and  $B^{Mo/S}$  stackings, must have contribution from the local AA stacking region alone. This leads to the localization of the VBM wave function around the  $O$  point, as shown in Fig. 4(a). In a similar manner, the VBM wave function of rigidly twisted  $M^{56.5}$  is localized to the  $B^{S/S}$  region or the  $B'$  point [Fig. 4(c)].

The equilibrium ILS in AA and  $B^{S/S}$  stackings is larger than other stackings [Fig. 2(a)]. This diminishes the hybridization between the two layers leading to a marked reduction in the splitting at the  $\Gamma$  point VBM as shown in Fig. 3(d). These splittings are now smaller than the other stackings [Figs. 3(e) and 3(f)]. As a result, the VBM of the AA and  $B^{S/S}$  stackings is now lower than the rest of the stackings. The VBM in relaxed  $M^{3.5}$  is then expected to originate from the local  $B^{S/Mo}$  and  $B^{Mo/S}$  regions. Figure 4(b) shows the VBM wave function in  $M^{3.5}$ , which is indeed localized at these regions, forming a hexagonal network. The localization pattern is significantly different from the rigidly twisted case, demonstrating the important role of atomic relaxations. The VBMs of AB and  $B^{Mo/Mo}$  stackings are close to each other (within  $\sim 0.1$  eV). Based on the band structures, the wave function is expected to lie at the  $B^{Mo/Mo}$  region in the MSL, since this stacking has a higher VBM level than AB. But the opposite localization is found in  $M^{56.5}$ , shown in Fig. 4(d), where the VBM is restricted to the AB ( $O'$  point) stacked regions. This is due to small tensile and compressive strains in the local  $B^{Mo/Mo}$  and AB regions, respectively. On taking this strain ( $\sim 0.3\%$ ) into account, the order of the VBM with respect to the vacuum level is reversed (see Supplemental Material [36]). The VBM thus localizes completely to the AB stacked regions [Fig. 4(d)]. Furthermore, the conduction band minimum (CBM) with

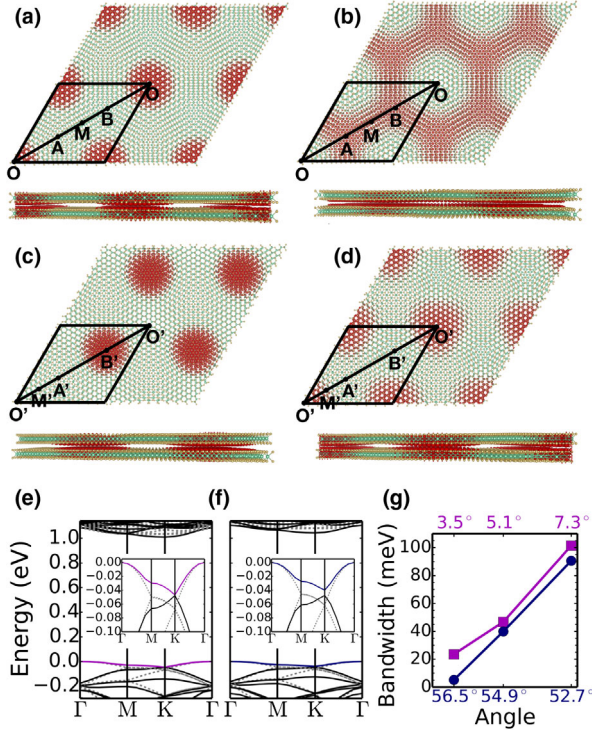


FIG. 4. Charge density of the VBM wave function in (a),(c) rigidly twisted [(b),(d) relaxed]  $M^{3.5}$  and  $M^{56.5}$ , respectively. The isosurface value for these plots is  $3 \times 10^{-4} e/\text{\AA}^3$ . (e),(f) Band structure of the relaxed  $M^{5.1}$  and  $M^{54.9}$ , respectively. The flatbands, near the valence band edge are shown with magenta and blue colors, respectively. The dashed line represents band structure of pure  $B^{M_0/S}$  and  $AB$  stacking for the same superlattice size, respectively. (Inset) An enlarged plot of the valence bands. (g) Variation of the bandwidth (in meV) with twist angle. The magenta line corresponds to angles approaching  $0^\circ$  and the blue line to angles approaching  $60^\circ$ .

respect to the vacuum level lines up among the stackings in Figs. 3(d)–3(f). Hence, no localization is found close to the CBM for  $M^{3.5}$  and  $M^{56.5}$ .

The localization of the VBM in the MSL is accompanied by flattening of the band in the TBZ. The band structure for TBLM in the TBZ for twist-angle  $5.1^\circ$ ,  $M^{5.1}$ , and  $54.9^\circ$ ,  $M^{54.9}$ , is shown in Figs. 4(e) and 4(f). The moiré bands close to the valence band edge are flatter than their pristine counterparts. Furthermore, a band gap opens at the  $K$  point in the TBZ for twist angles close to  $60^\circ$ . We define bandwidth,  $W$ , for the top valence band between the  $\Gamma$  and  $K$  point (see Supplemental Material [36] for comparison of the hole effective mass). Figure 4(h) shows the trend in  $W$  with twist angle. An ultraflatband with  $W = 5$  meV is formed in  $M^{56.5}$ , separated in energy from other valence states by 60 meV. The  $W$  for  $M^{3.5}$  is larger due to larger extent of real space localization, i.e., the formation of hexagonal networks rather than a spot.

We also estimate the on site Coulomb interaction  $U$  for  $M^{56.5}$  to be  $\sim 220$  meV. Computed using  $U = e^2/(4\pi\epsilon d)$ ,

TABLE I. VBM (in eV), with respect to the vacuum level, for the five stackings in other transition metal dichalcogenides:  $\text{MoSe}_2$ ,  $\text{WS}_2$ , and  $\text{WSe}_2$ .  $M$  stands for the transition metal and  $X$  for the chalcogen.

$MX_2$	AA	$B^{X/X}$	AB	$B^{M/X}$	$B^{M/M}$
$\text{MoSe}_2$	-5.06	-5.07	-4.70	-4.68	-4.73
$\text{WS}_2$	-5.34	-5.34	-4.93	-4.90	-4.87
$\text{WSe}_2$	-5.02	-5.04	-4.67	-4.73	-4.62

where  $d = 22$  Å from the charge density of the localized state and in-plane dielectric constant  $\epsilon = 3$  (see Supplemental Material [36]). A large ratio for  $U/W$  suggests the possibility of a Mott-insulator phase at half-filling of the band [17]. As discussed above, the conduction bands show no localization close to the Fermi level. The CBM is two-fold degenerate and delocalized in the MSL with weak interlayer hybridization. Hence, an external electric field in the out-of-plane direction can easily split these bands (see Supplemental Material [36]) and localize the CBM onto one of the layers [46].

We find that the bandwidth, localization of the flatband, and atomic relaxations do not change if a different exchange-correlation functional is used in the DFT calculations (see Supplemental Material [36]). We also find that the relative ordering of the VBM among the stackings, which determines the localization, remains the same in  $GW$  calculations [37,47] (see Supplemental Material [36]). Furthermore, we show that this feature is generic to other TMDs ( $MX_2$ ) by computing the VBM with respect to the vacuum level for the five high-symmetry stackings at the DFT level. The results are shown in Table I (see Supplemental Material [36] for band structures) for the equilibrium ILS. For all TMDs, the AA and  $B^{X/X}$  stackings have VBM levels about  $\sim 0.3$  eV below the VBMs of other stackings. The CBMs, on the other hand, line up among the stackings. We do not expect spin-orbit coupling to significantly alter our conclusions (see Supplemental Material [36]). Hence, we posit that a similar localization should occur at the valence band edge of these TMDs, in close resemblance to what we have shown for  $\text{MoS}_2$ .

In conclusion, we show the formation of ultraflat electronic bands close to the valence band edge in MSLs of TBLM. Our analysis of the origin of the flatband indicates that twisted bilayers of other TMDs must also show a flatband at the valence band edge. The spatial localization of electrons at the valence band edge will influence the binding energy and dynamics of excitons. The spatially varying band gap could lead to the formation of exciton funnels [48]. Doping the flatband with holes could lead to spin-liquid states, quantum anomalous Hall insulators, Mott-insulating phases, etc. at special filling factors [49]. Furthermore, the localization pattern of the flatband can be tuned with twist angle and is determined by atomic relaxations in the moiré pattern. The solitons can

be probed through scanning tunneling microscopy and transport measurements and could host topological edge states at small twist angles [50–52].

The authors thank Sumilan Banerjee, Arindam Ghosh, and H. R. Krishnamurthy for useful discussions. The authors thank the Supercomputer Education and Research Centre (SERC) at IISc for providing the computational facilities.

\*mjain@iisc.ac.in

- [1] J. S. Alden, A. W. Tsen, P. Y. Huang, R. Hovden, L. Brown, J. Park, D. A. Muller, and P. L. McEuen, *Proc. Natl. Acad. Sci. U.S.A.* **110**, 11256 (2013).
- [2] C. R. Woods *et al.*, *Nat. Phys.* **10**, 451 (2014).
- [3] M. Yankowitz, J. Xue, D. Cormode, J. D. Sanchez-Yamagishi, K. Watanabe, T. Taniguchi, P. Jarillo-Herrero, P. Jacquod, and B. J. LeRoy, *Nat. Phys.* **8**, 382 (2012).
- [4] M. Yankowitz, J. I. -J. Wang, A. G. Birdwell, Y.-A. Chen, K. Watanabe, T. Taniguchi, P. Jacquod, P. San-Jose, P. Jarillo-Herrero, and B. J. LeRoy, *Nat. Mater.* **13**, 786 (2014).
- [5] P. San-Jose, R. V. Gorbachev, A. K. Geim, K. S. Novoselov, and F. Guinea, *Nano Lett.* **14**, 2052 (2014).
- [6] G. Li, A. Luican, J. M. B. Lopes dos Santos, A. H. Castro Neto, A. Reina, J. Kong, and E. Y. Andrei, *Nat. Phys.* **6**, 109 (2010).
- [7] D. Wong, Y. Wang, J. Jung, S. Pezzini, A. M. DaSilva, H.-Z. Tsai, H. S. Jung, R. Khajeh, Y. Kim, J. Lee, S. Kahn, S. Tollabimazraehno, H. Rasool, K. Watanabe, T. Taniguchi, A. Zettl, S. Adam, A. H. MacDonald, and M. F. Crommie, *Phys. Rev. B* **92**, 155409 (2015).
- [8] P. San-Jose and E. Prada, *Phys. Rev. B* **88**, 121408 (2013).
- [9] E. Koren, I. Leven, E. Lörtscher, A. Knoll, O. Hod, and U. Duerig, *Nat. Nanotechnol.* **11**, 752 (2016).
- [10] H. Patel, R. W. Havener, L. Brown, Y. Liang, L. Yang, J. Park, and M. W. Graham, *Nano Lett.* **15**, 5932 (2015).
- [11] A. Ramires and J. L. Lado, *Phys. Rev. Lett.* **121**, 146801 (2018).
- [12] F. Gargiulo and O. V. Yazyev, *2D Mater.* **5**, 015019 (2018).
- [13] M. M. van Wijk, A. Schuring, M. I. Katsnelson, and A. Fasolino, *2D Mater.* **2**, 034010 (2015).
- [14] J. Kang, J. Li, S.-S. Li, J.-B. Xia, and L.-W. Wang, *Nano Lett.* **13**, 5485 (2013).
- [15] P. Kang, W.-T. Zhang, V. Michaud-Riou, X.-H. Kong, C. Hu, G.-H. Yu, and H. Guo, *Phys. Rev. B* **96**, 195406 (2017).
- [16] Y. Cao, V. Fatemi, S. Fang, K. Watanabe, T. Taniguchi, E. Kaxiras, and P. Jarillo-Herrero, *Nature (London)* **556**, 43 (2018).
- [17] Y. Cao, V. Fatemi, A. Demir, S. Fang, S. L. Tomarken, J. Y. Luo, J. D. Sanchez-Yamagishi, K. Watanabe, T. Taniguchi, E. Kaxiras, R. C. Ashoori, and P. Jarillo-Herrero, *Nature (London)* **556**, 80 (2018).
- [18] R. Bistritzer and A. H. MacDonald, *Proc. Natl. Acad. Sci. U.S.A.* **108**, 12233 (2011).
- [19] E. Suárez Morell, J. D. Correa, P. Vargas, M. Pacheco, and Z. Barticevic, *Phys. Rev. B* **82**, 121407 (2010).
- [20] K. F. Mak, C. Lee, J. Hone, J. Shan, and T. F. Heinz, *Phys. Rev. Lett.* **105**, 136805 (2010).
- [21] B. Radisavljevic, A. Radenovic, J. Brivio, V. Giacometti, and A. Kis, *Nat. Nanotechnol.* **6**, 147 (2011).
- [22] Q. H. Wang, K. Kalantar-Zadeh, A. Kis, J. N. Coleman, and M. S. Strano, *Nat. Nanotechnol.* **7**, 699 (2012).
- [23] K. Roy, M. Padmanabhan, S. Goswami, T. P. Sai, G. Ramalingam, S. Raghavan, and A. Ghosh, *Nat. Nanotechnol.* **8**, 826 (2013).
- [24] A. M. van der Zande, J. Kunstmann, A. Chernikov, D. A. Chenet, Y. You, X. Zhang, P. Y. Huang, T. C. Berkelbach, L. Wang, F. Zhang, M. S. Hybertsen, D. A. Muller, D. R. Reichman, T. F. Heinz, and J. C. Hone, *Nano Lett.* **14**, 3869 (2014).
- [25] S. Huang, X. Ling, L. Liang, J. Kong, H. Terrones, V. Meunier, and M. S. Dresselhaus, *Nano Lett.* **14**, 5500 (2014).
- [26] S. Huang, L. Liang, X. Ling, A. A. Purotzky, D. B. Geohegan, B. G. Sumpter, J. Kong, V. Meunier, and M. S. Dresselhaus, *Nano Lett.* **16**, 1435 (2016).
- [27] P.-C. Yeh, W. Jin, N. Zaki, J. Kunstmann, D. Chenet, G. Arefe, J. T. Sadowski, J. I. Dadap, P. Sutter, J. Hone, and R. M. Osgood, *Nano Lett.* **16**, 953 (2016).
- [28] K. Liu, L. Zhang, T. Cao, C. Jin, D. Qiu, Q. Zhou, A. Zettl, P. Yang, S. G. Louie, and F. Wang, *Nat. Commun.* **5**, 4966 (2014).
- [29] S. Carr, D. Massatt, S. Fang, P. Cazeaux, M. Luskin, and E. Kaxiras, *Phys. Rev. B* **95**, 075420 (2017).
- [30] M.-L. Lin, Q.-H. Tan, J.-B. Wu, X.-S. Chen, J.-H. Wang, Y.-H. Pan, X. Zhang, X. Cong, J. Zhang, W. Ji, P.-A. Hu, K.-H. Liu, and P.-H. Tan, *ACS Nano* **12**, 8770 (2018).
- [31] W. Kohn and L. J. Sham, *Phys. Rev.* **140**, A1133 (1965).
- [32] P. Giannozzi *et al.*, *J. Phys. Condens. Matter* **21**, 395502 (2009).
- [33] E. J. Mele, *Phys. Rev. B* **81**, 161405 (2010).
- [34] J. M. B. Lopes dos Santos, N. M. R. Peres, and A. H. Castro Neto, *Phys. Rev. Lett.* **99**, 256802 (2007).
- [35] <http://www.physics.iisc.ernet.in/~mjain/pages/software.html>.
- [36] See Supplemental Material at <http://link.aps.org/supplemental/10.1103/PhysRevLett.121.266401> for details on constructing the MSL, including Refs. [34,35], and details of the DFT and *GW* calculations, including Refs. [37–44].
- [37] M. S. Hybertsen and S. G. Louie, *Phys. Rev. B* **34**, 5390 (1986).
- [38] J. P. Perdew and A. Zunger, *Phys. Rev. B* **23**, 5048 (1981).
- [39] S. Grimme, *J. Comput. Chem.* **27**, 1787 (2006).
- [40] J. Deslippe, G. Samsonidze, D. A. Strubbe, M. Jain, M. L. Cohen, and S. G. Louie, *Comput. Phys. Commun.* **183**, 1269 (2012).
- [41] M. Rohlfing and S. G. Louie, *Phys. Rev. B* **62**, 4927 (2000).
- [42] S. Ismail-Beigi, *Phys. Rev. B* **73**, 233103 (2006).
- [43] J. Deslippe, G. Samsonidze, M. Jain, M. L. Cohen, and S. G. Louie, *Phys. Rev. B* **87**, 165124 (2013).
- [44] J. P. Perdew, M. Ernzerhof, and K. Burke, *J. Chem. Phys.* **105**, 9982 (1996).
- [45] M. H. Naik and M. Jain, *Phys. Rev. B* **95**, 165125 (2017).
- [46] T. Cao, Z. Li, D. Y. Qiu, and S. G. Louie, *Nano Lett.* **16**, 5542 (2016).
- [47] L. Hedin, *Phys. Rev.* **139**, A796 (1965).
- [48] M. Wu, X. Qian, and J. Li, *Nano Lett.* **14**, 5350 (2014).
- [49] F. Wu, T. Lovorn, E. Tutuc, and A. H. MacDonald, *Phys. Rev. Lett.* **121**, 026402 (2018).

- [50] L.-J. Yin, H. Jiang, J.-B. Qiao, and L. He, *Nat. Commun.* **7**, 11760 (2016).
- [51] A. Vaezi, Y. Liang, D. H. Ngai, L. Yang, and E.-A. Kim, *Phys. Rev. X* **3**, 021018 (2013).
- [52] L. Ju, Z. Shi, N. Nair, Y. Lv, C. Jin, J. Velasco, Jr., C. Ojeda-Aristizabal, H. A. Bechtel, M. C. Martin, A. Zettl, J. Analytis, and F. Wang, *Nature (London)* **520**, 650 (2015).